

Performance and High-Speed Characterization of a 100-kW Nested Hall Thruster

Scott J. Hall^{*}, Benjamin A. Jorns[†], Sarah E. Cusson[‡] and Alec D. Gallimore[§]
University of Michigan, Ann Arbor, MI, 48109, USA

Hani Kamhawi[¶], Peter Y. Peterson^{||}, Thomas W. Haag^{**}, and Jonathan A. Mackey^{††}
NASA Glenn Research Center, Cleveland, OH, 44135, USA

Matthew J. Baird^{‡‡}
Western Michigan University, Kalamazoo, MI, 49008, USA

James H. Gilland^{§§}
Ohio Aerospace Institute, Brookpark, OH, 44142, USA

The performance of a three-channel, 100-kW nested Hall thruster was evaluated on xenon propellant for total powers up to 102 kW. The thruster demonstrated stable operation in all seven available channel combinations at discharge voltages from 300 V to 500 V and three different current densities. The resulting test matrix contained forty-six unique conditions ranging from 5 to 102 kW total power and 16 to 247 A discharge current. At each operating condition, thrust, specific impulse, and efficiency were characterized. All seven channel combinations showed similar performance at a given discharge voltage and current density. The largest thrust recorded was $5.4 \text{ N} \pm 0.1 \text{ N}$ at 99 kW/400 V discharge voltage. Total efficiency and specific impulse ranged from 0.54 to 0.67 ± 0.03 and 1800 seconds to $2650 \text{ seconds} \pm 60 \text{ seconds}$, respectively. Discharge current oscillations were also characterized with peak-to-peak values and with high-speed camera analysis, which provide insight into how the discharge channels oscillate, and how those oscillations are affected by the presence of other operating channels. These results are discussed in the context of differences between single- and multi-channel operation, as are the implications for the general viability of nested Hall thruster technology for future mission applications.

^{*}Ph.D. Candidate, Department of Aerospace Engineering. Currently: Research Engineer, Electric Propulsion Systems Branch, HX5, LLC, NASA Glenn Research Center, scott.j.hall@nasa.gov, Member, AIAA

[†]Assistant Professor, Department of Aerospace Engineering, bjorns@umich.edu, Senior Member, AIAA.

[‡]Ph.D. Candidate, Department of Aerospace Engineering, cusson@umich.edu, Student Member, AIAA.

[§]Robert J. Vlasic Dean of Engineering, Richard F. and Eleanor A. Towner Professor, and Arthur F. Thurnau Professor, Department of Aerospace Engineering, alec.gallimore@umich.edu, Fellow, AIAA.

[¶]Senior Research Engineer, Electric Propulsion Systems Branch, hani.kamhawi-1@nasa.gov, Associate Fellow, AIAA.

^{||}Senior Research Engineer, Electric Propulsion Systems Branch, peter.y.peterson@nasa.gov, Associate Fellow, AIAA.

^{**}Research Engineer, Electric Propulsion Systems Branch, thomas.w.haag@nasa.gov, Member, AIAA.

^{††}Research Engineer, Electric Propulsion Systems Branch, jonathan.a.mackey@nasa.gov, Member, AIAA.

^{‡‡}Ph.D. Candidate, Department of Mechanical and Aerospace Engineering, matthew.j.baird@wmich.edu, Student Member, AIAA.

^{§§}Research Engineer, Electric Propulsion Systems Branch, james.h.gilland@nasa.gov, Associate Fellow, AIAA.

Nomenclature

g Earth's gravitational acceleration, 9.81 m/s^2

I current, A

j current density, mA/cm^2

m oscillation mode

\dot{m} mass flow rate, mg/s

p pressure, Torr

P power, kW

T thrust, N

T/P thrust-to-power ratio, mN/kW

TCFF total cathode flow fraction

V voltage, V

η efficiency

Subscripts

a anode

b background

c cathode

d discharge

I Inner channel

inj injector

$keep$ keeper

M Middle channel

mag magnet

O Outer channel

$P2P$ peak to peak

ref reference

RMS root mean square

t total

I. Introduction

THE next generation of electric propulsion (EP) systems—those in excess of 300 kW—can enable missions ranging from station-keeping of large Earth satellites to crew transport to Mars. Multi-hundred-kW EP systems can reduce LEO-to-GEO orbit transfer times to be comparable to chemical propulsion systems while allowing for nearly double the payload capability. Mission studies have demonstrated the need for 300-kW EP systems for mission applications such as station-keeping of large Earth satellites and for cargo tugs for crewed missions to locations such as Earth-Moon space and near-Earth asteroids, and that EP systems in excess of 600 kW would enable cargo or crew transport to Mars and its moons [1]. These systems would reduce trip times and increase deliverable payload. For crewed missions to these bodies and others, high-power EP systems offer benefits in trip time and payload capability that can increase astronaut time on the surface and reduce the number of launches necessary for a given mission.

While the need for high-power EP is apparent, there are multiple ways in which these systems could be realized. For example, a 300-kW system could consist of one large 300-kW thruster or an array of ten smaller 30-kW thrusters. The question of which configuration is optimum is one of cost, mass, performance, and footprint. Recent work performed a systematic analysis of this question, taking real Hall thruster information from laboratory and flight programs to study propulsion system mass and cost trends [2]. A major conclusion of that work was that 50 to 100-kW EP devices are an optimal building block for missions up to 1-MW of total propulsion power. This covers all but the most ambitious future missions and strongly suggests the need to focus development efforts on thrusters of this class.

Hall thrusters are an attractive EP technology to be scaled to 50 to 100-kW-class devices for these high-power missions. Mission analysis has demonstrated that specific impulses on the order of 1500-2000 seconds are optimal to reduce trip times for human crews. Hall thrusters are capable of total efficiencies in excess of 60% for these conditions [3]. Efforts to scale Hall thrusters to these power levels in the United States have been underway for over 20 years. This work culminated in a series of 20-50 kW class Hall thrusters that demonstrated for the first time the performance capability of this technology at these power levels. The 50-kW class NASA-457Mv1 thruster, the highest-power thruster produced from this effort, was operated on xenon and krypton propellants through a range of operating conditions, demonstrating on xenon propellant a maximum total power of 96 kW, maximum discharge current of 112 A, maximum total efficiency of 0.58, and specific impulses from 1550-3560 seconds [4]. This thruster demonstrated scaling techniques and physical insight for creating high-power Hall thrusters. Leveraging this work, a higher-fidelity version of the thruster named the NASA-457Mv2 was developed, which demonstrated improved performance over the v1 thruster [5], though it was not tested beyond 50 kW discharge power. Additionally, the NASA-300M 20-kW thruster and NASA-400M 50-kW thruster were developed using similar scaling techniques, applying design lessons learned to continually improve performance [6, 7]. This culminated in a demonstrated peak total efficiency of 0.67 at 500 V, 20 kW with the NASA-300M on xenon propellant. A 150-kW single-channel Hall thruster was even designed using these techniques but never built [8]. This thruster, designated the NASA-1000M, would have been 1 meter in diameter, the largest Hall thruster ever built.

While this effort was highly successful and demonstrated a road map toward 150-kW Hall thruster systems, one of the major challenges identified (and exemplified by the NASA-1000M thruster design) was the excessively large footprint of higher-power systems. This is due to the fact that thruster diameter increases with power using these scaling techniques. One technique to avoid this issue and scale Hall thrusters beyond 50-kW class devices while limiting diameter increase is to concentrically nest multiple discharge channels around a shared centrally-mounted cathode. This approach allows for improved packing density of the channels as compared to multiple single-channel thrusters [1] while still relying on proven channel scaling techniques. Initial exploration of this concept was performed with two 10-kW class nested Hall thrusters (NHTs) [9, 10]. One of these thrusters, known as the X2, demonstrated the feasibility of multiple nested magnetic lens topologies and operation of multiple discharge channels from a single shared cathode, and it generally forged a path for continued NHT development. Building off of that success, in 2009, development began of a three-channel, 100-kW class NHT known as the X3 [11, 12]. This thruster capitalized not only on the success of the X2 NHT but on the aforementioned series of high-power single channel Hall thrusters. The X3 was first fired in 2013, but due to facility limitations, early characterization of the thruster was limited to 30 kW [1, 11].

Though NHTs have shown promise, there still exist questions about the performance and high-power capability of the technology. The X2 displayed anode efficiencies in excess of 60% during its characterization but was only throttled to 500 V discharge voltage. The 30-kW characterization of the X3 showed surprisingly low performance for the larger channels. There also remain questions regarding the mechanisms through which channels couple to one another. Early work on both the X2 and X3 showed cross-talk between channels, but thorough investigation was not undertaken. Thus, the need is apparent to continue the development of NHTs, starting with characterizing the X3 at current densities and powers closer to nominal values.

In this paper we focus on the performance mapping of the X3. In Section II, we discuss the test apparatus. Section III presents the measured thrust as well as calculated efficiency and specific impulse values. These results are presented in the context of other high-power Hall thrusters to show how the X3's behavior and trends compare to the state of the art. In Section IV, discharge current oscillation behavior is studied using data collected from a high-speed camera. Finally, the performance and oscillation results are discussed in the context of differences between single- and multi-channel operation in Section V. In a companion paper, we present data collected from an array of plasma plume diagnostics [13].

II. Experimental Apparatus

A. The X3 NHT

The X3 is a three-channel 100-kW class NHT. The X3 is designed to operate efficiently on both krypton and xenon propellants from 200–800 V discharge voltage and at total discharge currents up to 250 A. The total power throttling range of the X3 is 2–200 kW. Throughout this paper, we define total power as the total thruster input power, which

includes the discharge power to all operating channels, the input power to all operating electromagnets, and any power drawn by the cathode keeper. The thruster is approximately 80 cm in diameter and weighs 230 kg. Each of the three discharge channels features an inner and outer electromagnet for a total of six, each of which is controlled separately. Due to the shared poles between adjacent channels, the magnetic field direction alternates, such that the Middle channel's field points in the opposite direction as the Inner and Outer channels.

Each of the X3's discharge channels can be fired separately or in combination with others, providing seven unique operating configurations. We denote these configurations throughout this paper using I for the innermost channel, M for the middle channel, and O for the outermost channel. For example, the configuration where the Inner and Middle channels are firing together is denoted as the IM configuration. The thruster operates off of a single high-current cathode capable of discharge currents in excess of 300 A. It features a lanthanum hexaboride (LaB_6) emitter and unique external gas injectors that reduce energetic ion production [14]. The total cathode flow fraction (TCFF) for this cathode is split between the cathode center and the injectors:

$$\text{TCFF} = \frac{\dot{m}_{c,t}}{\dot{m}_{a,t}} = \frac{\dot{m}_c + \dot{m}_{inj}}{\dot{m}_{a,I} + \dot{m}_{a,M} + \dot{m}_{a,O}}, \quad (1)$$

where $\dot{m}_{c,t}$ is the total cathode flow rate, $\dot{m}_{a,t}$ is the total anode flow rate, \dot{m}_c is the cathode center flow rate, \dot{m}_{inj} is the cathode injector flow rate, and $\dot{m}_{a,i}$ is the anode flow rate for discharge channel i . Work has identified 1.56 mg/s of xenon as the optimized flow rate for the cathode center (\dot{m}_c), so any remainder of the TCFF is flowed through the external injectors. For all but one test point here, the cathode was operated at a TCFF of 7% of the total anode flow (one test point was at 5%). Elsewhere, low-cathode flow fraction operation was demonstrated with the X3 and this cathode [15], but for this study we maintained more traditional cathode flow fractions for better comparison with state of the art.

During this test campaign, the X3 was electrically isolated from the thrust stand inside the vacuum facility but then tied to facility ground on the atmosphere side of the test setup with a dedicated body grounding strap. The current collected by the grounded body was then recorded during testing. Throughout testing, including operation at 250 A discharge current, the collected body current did not exceed 1.25 A.

B. Vacuum Facility and Test Equipment

The testing described here was performed in VF-5 at NASA Glenn Research Center (GRC). A schematic of the experimental apparatus is shown in Figure 1. VF-5 is a 4.6 m diameter, 18.3 m long cylindrical vacuum chamber that features 33 m² of cryogenic pump surfaces, providing a pumping speed of 700,000 L/s on xenon. The facility walls and cryogenic panels are lined with graphite plates to minimize backscatter during thruster operation. Pressure inside the facility was monitored using a hot-cathode ionization gauge mounted in the exit plane of the thruster, approximately 1.5 meters from thruster centerline and pointed downstream, per industry best practices [16]. This gauge was calibrated on

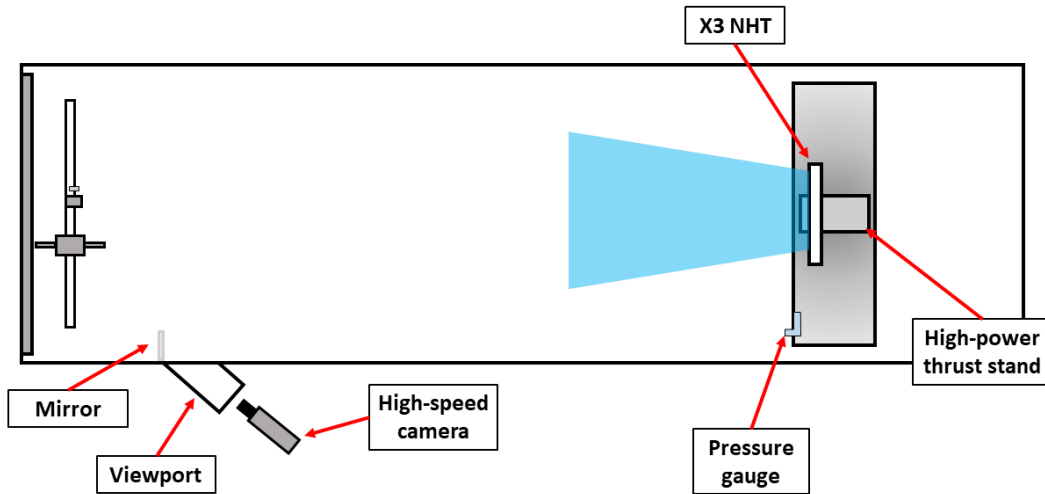


Fig. 1 A schematic of the experimental apparatus. Drawing is not to scale.

xenon and was corrected for orientation. Facility base pressures were typically on the order of 1×10^{-7} Torr during this test campaign. Orientation-corrected background pressures while firing the thruster ranged from 4.3×10^{-6} to 4.2×10^{-5} Torr.

We operated the thruster off of a set of laboratory power supplies, which included six separate supplies for the electromagnets, a cathode heater supply, and a cathode keeper supply. Each of the three channels was operated from a separate high-voltage, high-current power supply. The Inner was operated using a set of three 1000 V, 15 A supplies that were connected in parallel, the Middle was operated using a 2000 V, 100 A supply, and the Outer channel was operated using a 1000 V, 150 A supply. Each discharge channel featured a 100 μ F capacitor across the anode and cathode lines. These capacitors isolated the power supplies from the thruster. Electric propulsion-grade xenon propellant was provided to the thruster via five electropolished stainless steel feed lines. Each line featured a precision flow controller to supply the xenon, sized for the flow rate range necessary for the component it supplied (Inner channel, Middle channel, Outer channel, cathode center, and external cathode injectors).

We measured thruster telemetry in a breakout box that contained precision shunts, voltage dividers, and isolation amplifiers. This telemetry was collected by a LabView data logger. Telemetry was recorded at a rate of approximately 0.3 Hz. In addition to the low-speed measurements taken in the breakout box, high-speed measurements of the discharge currents were taken using a set of clamp-on current probes read by two oscilloscopes. The discharge current oscillations were characterized using peak to peak (P2P) and root mean square (RMS) values that were calculated by the oscilloscopes and read by the telemetry data logger. Additionally, synchronized with acquisition of high-speed video as described below, we collected high-speed measurements of the discharge current of each channel, which were used for power

spectral density analysis of the dominant oscillation frequencies.

C. Thrust Stand

We designed and built a new inverted-pendulum thrust stand capable of measuring up to 8 N of thrust for this test campaign. The stand was based heavily on the X3-dedicated thrust stand developed by Hall previously [1]. The thrust stand operates in null mode, is calibrated in situ using a string of known masses, has active inclination control, and is water-cooled to protect against thermal drift during thruster operation, following industry best practices [17–19].

Based on data collected throughout the test, the thrust stand was found to have a statistical uncertainty of approximately 2% of the measurement, plus an additional 14 mN uncertainty due to the resolution of the inclination reading. We performed in-situ calibrations of the stand at the beginning and end of each test day, and additionally took zeros periodically throughout the day. Over the course of this weeks-long test campaign, we found that the thrust stand calibration slope (in mN/V) varied around the mean with a standard deviation of about 2%. Thermal drift of the measurement zero was typically around 1-2% of full scale across a day of operation and was corrected out of the measurement using best practices [19].

D. High Speed Camera

The high-speed oscillatory behavior of a Hall thruster is a critical aspect of its operation [20–24]. As such, synchronized with the acquisition of high-speed discharge current measurements with the clamp-on probes and oscilloscopes described above, we recorded video of the thruster discharge using a high-speed camera (HSC). The HSC was positioned at a viewport on the atmosphere side of VF-5, and a mirror was placed inside the chamber and aligned such that the HSC could see the thruster nearly head-on. At each test condition, the HSC was adjusted such that the entire discharge was captured. The HSC was operated at a frame rate of 180 kfps with an image size of 256 pixels by 256 pixels.

For HSC data analysis we followed a procedure that was originally developed by McDonald [25], expanded by Sekerak [22], and used by others [23]. Here, we extend the technique to accommodate up to three simultaneously operating discharge channels. Figure 2 shows a sequence of Inner, Middle, and Outer channel curve fit sets used to identify each operating discharge channel, shown for an example three-channel operating condition.

The data analysis followed a series of steps, detailed further by Hall [1], which included the ellipse fitting routine illustrated by Figure 2, a bin-and-average technique performed on each frame, and the computation from these data of a $\phi - t$ or spoke surface plot and power spectral densities for each oscillation mode. Following McDonald [25], the mode number m is defined as the number of localized bright spots in the discharge channel. Thus the $m = 0$ mode corresponds to the entire discharge channel oscillating in time, the $m = 1$ mode corresponds to a single spoke or localized bright spot propagating around the channel, etc.). Results from this analysis provide insight into how the thruster oscillations are

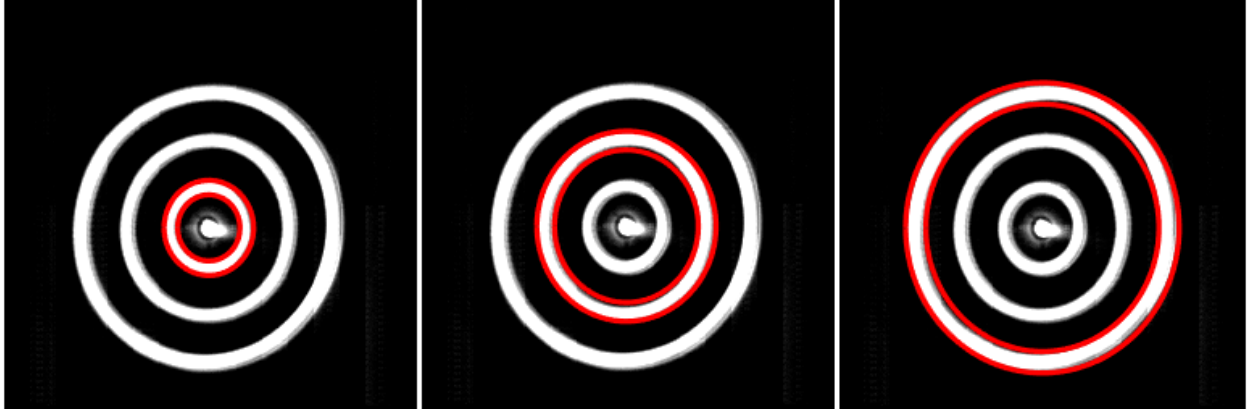


Fig. 2 Example ellipses fit to identify the Inner (left), Middle (center), and Outer (right) discharge channels from the same mean image. This technique was applied to all multi-channel conditions to isolate each channel.

changing across the throttle table.

III. Performance

We successfully operated the X3 across a throttling envelope spanning 300–500 V discharge voltage and three current densities (defined here as the discharge current of a given channel divided by the exit area of the channel). Using the intermediate value as reference, these current densities were 0.63, 1.00, and 1.26 the reference value j_{ref} . All seven possible thruster configurations (I, M, O, IM, IO, MO, and IMO) were tested at each discharge voltage for the $0.63j_{ref}$ and $1.00j_{ref}$ conditions. For all test points, all operating channels were held at the same discharge voltage and current density. Additional test points were collected at 300 V and 400 V at the $1.26j_{ref}$ condition, bringing the total unique test conditions to 46 for this performance characterization. We designed the test matrix to study the performance trends with both discharge voltage and current density, as well as to study how the performance varies for different channel combinations at fixed values of these parameters. Throttle tables for 300, 400, and 500 V conditions are presented in the appendix for reference.

A. Thruster Operation

For all performance calculations here, the thruster was allowed to settle until the mean discharge current of each channel changed no more than 0.01 A/min. We did not allow the thruster to come into thermal steady state during these measurements due to the necessary length of time (expected to be in excess of 6 hours depending on the operating point). This concession is one made previously with large high-power Hall thrusters [4]. Hours-long continuous operation at 50 and 80 kW indicated thruster performance and behavior did not change significantly with temperature. However, each channel of the X3 was thoroughly conditioned at a given power level prior to any performance measurements at that power level.

At each condition, we performed limited magnetic field mapping before collecting the performance data. We varied the magnetic field strength while maintaining the field shape, as is typical for Hall thrusters. The anode flow rate was held constant during the magnetic field map. During a sweep, thruster discharge, oscillation, and performance parameters were monitored. The optimal field strength for a given condition was that which provided the minimum discharge current. Typical sweep ranges were from 0.8 to 1.3 the reference field strength. Previous X3 field sweeps were more extensive, and because the sweeps during this campaign matched the trends of those previous results we did not extend our range here [1]. The reference field strength was the same for each channel and did not vary between single- and multi-channel conditions, although the magnet coil current ratios had to be modified in multi-channel operation. Optimized field strengths across all conditions did not vary by more than 30%. Upon identification of the optimized field strength, the anode flow rate was adjusted to achieve the target discharge current if necessary prior to taking performance measurements.

Due to the complexities involved in multi-channel magnetic field optimization (where the field of each channel affects the others), only minimal efforts to optimize the field were undertaken for multi-channel conditions. Typically, multi-channel conditions were simply operated at or near the optimum magnetic field strength found for single-channel operation at the given discharge voltage and current density. The field strength was kept constant across all firing channels for multi-channel operation. Because of this, we speculate that further performance improvements through magnetic field tuning may be possible for the multi-channel conditions, as will be discussed below.

B. Thruster Performance

Thruster performance is evaluated here using both anode and total quantities. The anode values provide an opportunity to compare thruster behavior while removing the electromagnets and cathode, neither of which has been optimized for flight, and the total values provide insight into how the X3 thruster would fit into system-level operation.

Anode efficiency is calculated as

$$\eta_a = \frac{T^2}{2\dot{m}_{a,t}P_{d,t}}, \quad (2)$$

where T is the measured thrust, $\dot{m}_{a,t}$ is total anode mass flow rate, and $P_{d,t}$ is total discharge power. Both $\dot{m}_{a,t}$ and $P_{d,t}$ are summed across all firing channels. Anode specific impulse is calculated as

$$I_{sp,a} = \frac{T}{\dot{m}_{a,t}g}, \quad (3)$$

where g is Earth's gravitational acceleration, 9.81 m/s^2 .

Total values of efficiency and specific impulse are calculated very similarly to anode quantities, except that they include extra terms for the cathode and electromagnets. Total thruster efficiency is calculated as

$$\eta_t = \frac{T^2}{2\dot{m}_t P_t}, \quad (4)$$

where \dot{m}_t is total mass flow rate:

$$\dot{m}_t = \dot{m}_{a,t} + \dot{m}_{c,t} \quad (5)$$

and P_t is total power:

$$P_t = P_{d,t} + P_{mag} + P_{keep}. \quad (6)$$

In Equation 5, $\dot{m}_{c,t}$ is total cathode mass flow rate (as described in Equation 1), and in Equation 6, P_{mag} is power to the electromagnets and P_{keep} is power to the keeper, which was used at certain low-power conditions to stabilize the discharge. Total thruster specific impulse is then calculated as:

$$I_{sp,t} = \frac{T}{\dot{m}_t g}. \quad (7)$$

Thruster telemetry values used in these calculations were averaged over a 60-second period.

The uncertainty in the thrust measurement was the dominant contribution to the uncertainty in efficiency and specific impulse calculations. Because the thrust uncertainty increased at lower thrust values (due to the constant-value uncertainty from the inclination resolution), lower-power conditions typically had slightly larger uncertainties in efficiency and specific impulse as well. Average uncertainties for specific impulse were ± 40 s and for efficiency were ± 0.04 . Inner channel conditions typically were closer to ± 100 s and ± 0.06 because of their higher relative thrust uncertainty. These uncertainties are reflected in the error bars on the plots below.

Figure 3 presents thrust as a function of discharge power. For the conditions tested, the X3 produced a maximum thrust of 5.42 N (± 0.1 N) at 98.4 kW discharge power (400 V, 247 A). At 101 kW discharge power (500 V, 201 A) the X3 produced 5.03 N (± 0.1 N). At a fixed discharge voltage, the X3 operated at a similar thrust to power ratio (T/P) in each of the seven channel combinations. Because of the large number of channel combinations for the X3, these different configurations are not noted in these figures for clarity. Average T/P values are plotted alongside the data in the figure and are additionally compared to those of other NASA high-power Hall thrusters in Table 1. As shown in the table, the average T/P results are slightly improved over those of other high-power Hall thrusters, indicating that the X3 is operating as designed. These results also demonstrate that the T/P value attained is not dependent on the channel combination.

Figure 4 shows anode and total specific impulse as a function of discharge power. We found that the anode specific impulse for the conditions tested ranged from 1930–2150 seconds (± 50 seconds) for 300 V, 2190–2470 seconds (± 50

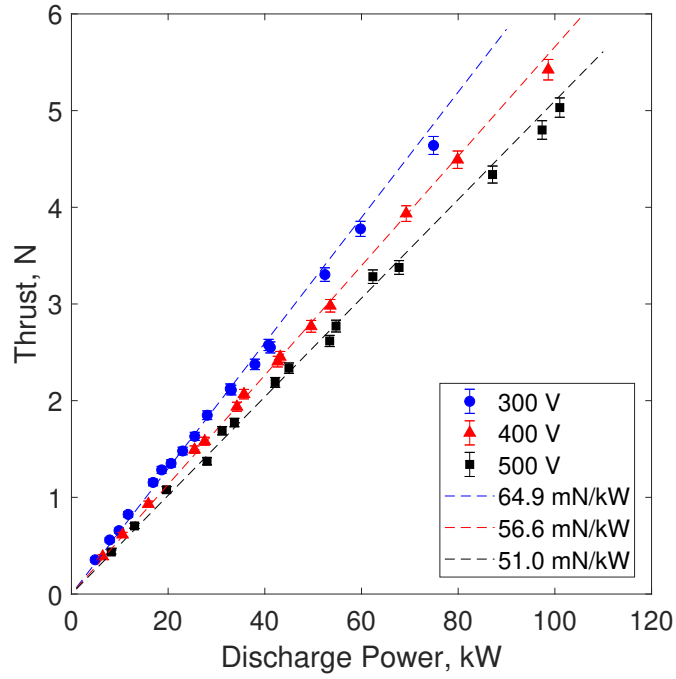


Fig. 3 X3 thrust versus total discharge power.

Table 1 The average thrust-to-power values for the X3 and other NASA high-power Hall thrusters for each discharge voltage tested.

V_d	NASA-457Mv1	NASA-400M	NASA-300M	X3 NHT
300 V	57.8 mN/kW	59.0 mN/kW	63 mN/kW	64.9 mN/kW
400 V	51.9 mN/kW	49.7 mN/kW	56 mN/kW	56.6 mN/kW
500 V	47.2 mN/kW	47.4 mN/kW	50 mN/kW	51.0 mN/kW

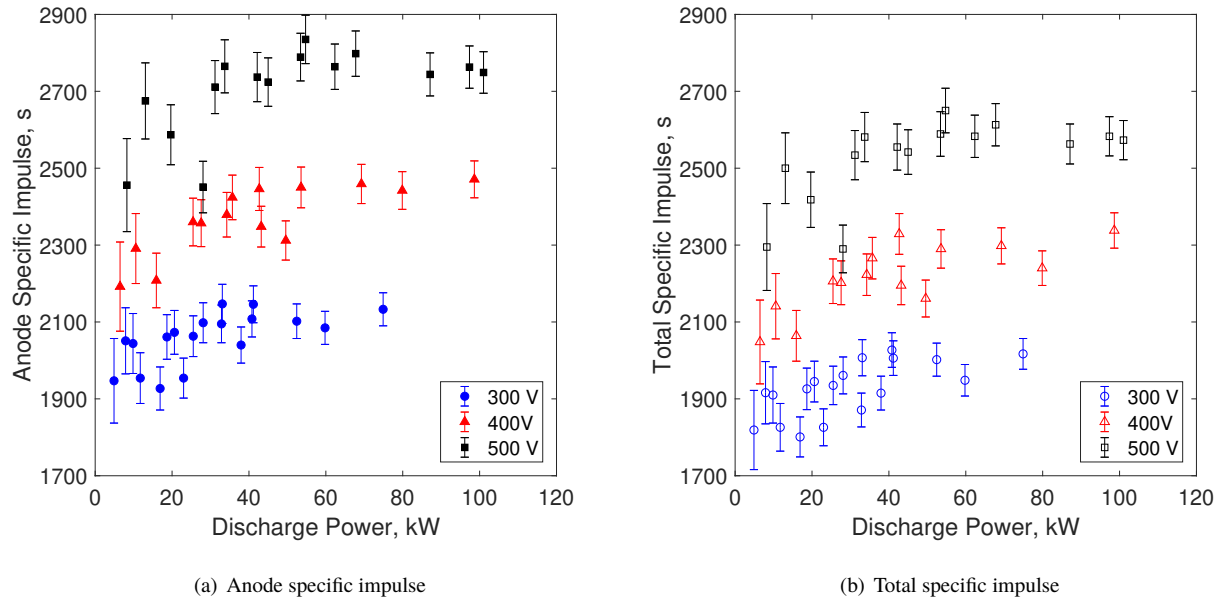


Fig. 4 X3 specific impulse as a function of discharge power for different discharge voltages.

Table 2 Comparison of anode specific impulse ranges at different discharge voltages from the X3 and other NASA high-power Hall thrusters.

V_d	NASA-457Mv1	NASA-400M	NASA-300M	X3 NHT
300 V	1750–2100 s	1700–2100 s	1900–2200 s	1930–2150 s
400 V	2100–2400 s	2000–2600 s	2200–2600 s	2190–2470 s
500 V	2400–2750 s	2500–3000 s	2500–2900 s	2480–2840 s

seconds) for 400 V, and 2480–2840 seconds (± 60 seconds) for 500 V, and that except for a slight decrease at low power (less than approximately 20 kW), specific impulse for a given discharge voltage was constant with discharge power, regardless of channel combination. The X3’s values match those found for other high-power Hall thrusters, as shown in the anode specific impulse ranges presented in Table 2.

Table 3 presents the anode efficiency ranges and averages for the X3 versus discharge voltage, as well as ranges for other high-power Hall thrusters. Anode efficiency is used for this comparison because total efficiency values were not published for all other thrusters. It can be seen that the average efficiency of the X3 increases with increasing discharge voltage, a trend shared with the other thrusters.

During this test, the X3 operated at a peak total efficiency of 0.64 (± 0.03) at 400 V and 0.67 (± 0.03) at 500 V. In general, the total efficiency was approximately 0.05 lower than anode efficiency regardless of operating configuration. For reference, the NASA-300M demonstrated peak total efficiencies of 0.67 at 400 V and 0.66 at 500 V. Thus, it is apparent that the X3 is operating at the state of the art, and continued magnetic field optimization may even further increase these values.

Table 3 Comparison of anode efficiency ranges at different discharge voltages from the X3 and other NASA high-power Hall thrusters.

V_d	NASA-457Mv1	NASA-400M	NASA-300M	X3 NHT range	X3 NHT avg.
300 V	0.50–0.57	0.55–0.59	0.60–0.67	0.62–0.71	0.66
400 V	0.53–0.60	0.60–0.65	0.55–0.73	0.63–0.71	0.66
500 V	0.46–0.65	0.66–0.71	0.60–0.73	0.58–0.72	0.68

IV. High Speed Discharge Behavior

Discharge current oscillations have been shown to affect Hall thruster performance [24] and their effects have been proposed to have roles in thruster processes such as anomalous transport [21, 26] and cathode erosion [27]. As such, measuring these oscillations in the X3 was an important part of this thruster characterization effort. We used both the high-speed camera and the clamp-on current sensors for this, the results from which are presented below.

A. High Speed Camera

1. Overview of Results

As an example of typical HSC results, we present in Figure 5 a power spectral density (PSD) and ϕ -t or spoke-surface plot for the Inner channel operating at 400 V, $1.0j_{ref}$. In the PSD, the black trace represents the $m=0$ mode or the breathing mode; the red and orange traces represent spoke modes of increasing m . In this example trace, as for all channels in all operating conditions, the $m=0$ breathing mode is the dominant oscillation characteristic. The $m=2$ and 3 spoke modes (and modes of higher m up to $m=6$, which are not shown for clarity) feature no distinguishing peaks and are 1-2 orders of magnitude lower in power than the $m=0$ mode. In some cases, the higher- m traces exhibited peaks at identical frequencies to the $m=0$ mode, but for all cases these modes were one or more orders of magnitude lower in power than the $m=0$ mode, indicating that this breathing mode was dominant. In the example FFT, a strong peak on the order of 10 kHz can be seen, with a lower-magnitude, broader peak closer to 70 kHz. A low-frequency peak on the order of 10 kHz was present in all $m=0$ results for all conditions, and a high-frequency peak on the order of 60-80 kHz was typically present, but the strength of this high-frequency peak relative to the low-frequency peak varied with operating condition.

The dominance of the $m=0$ breathing mode is reflected in the example ϕ -t plot shown in Figure 5. The vertical striations in the plot indicate that for a given time, the entire discharge channel was at approximately constant brightness, and that the brightness was changing uniformly across the whole discharge channel. Unlike previous work on the H6 Hall thruster [24], the oscillations in the X3 appear to vary in strength with time. Sekerak’s example breathing mode was consistent and sinusoidal, whereas the X3 oscillations vary in strength and are not evenly spaced temporally. This behavior is also captured in the relative broadness of the low-frequency peak (with a full-width half-maximum of approximately 10 kHz). A distinctly sinusoidal oscillation would be reflected instead with a sharp peak at the oscillation

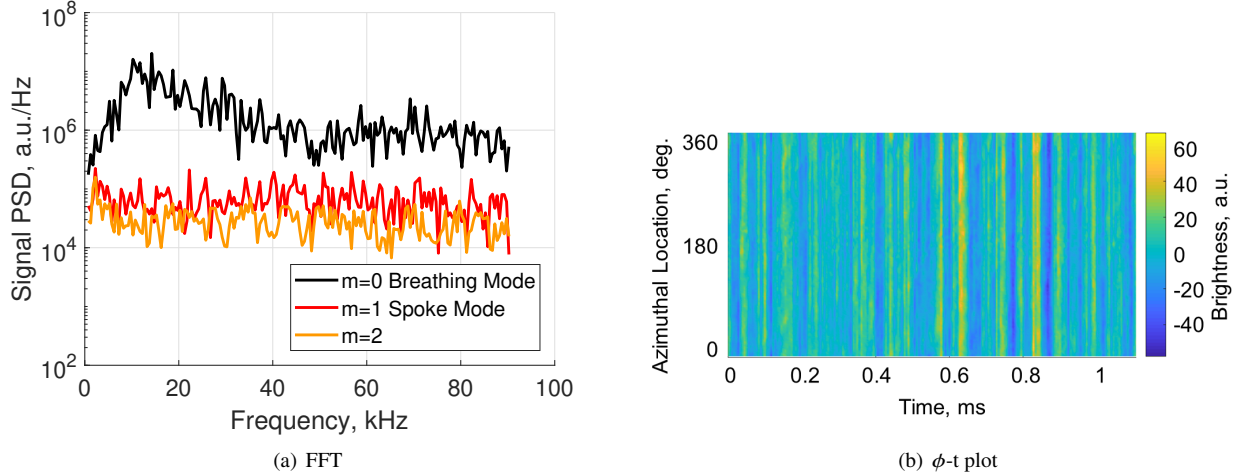


Fig. 5 Example HSC results for the Inner channel at 400 V, $1.0 j_{ref}$.

frequency.

Generally, these example results are very similar to those found for the Middle and Outer channels, and for all three channels operating both separately and in multi-channel operation. The only feature that showed a distinct difference between channels was the frequency of the peaks in the PSDs, which we discuss below. In some conditions both when operating alone or with other channels, the Middle and Outer channels would display faint diagonal striations as well, indicating spoke features. These striations would appear in only one location in the channel and propagate over a range of approximately 60 degrees of the channel face before disappearing. For both the Middle and Outer channels, these features propagated in that channel's $\vec{E} \times \vec{B}$ direction (which, due to the magnetic field of the thruster, were opposite directions). Work on the H6 thruster demonstrated that spokes propagated in the $\vec{E} \times \vec{B}$ direction and changed directions when the magnetic field direction was reversed on that thruster [22]. Because these features were not dominant, they did not factor into our analysis. Plots of these conditions can be found in Hall [1]. Altogether, the results of the HSC analysis suggest that all three channels, whether operating separately or together, are operating in a very similar mode.

2. Correlation Between Channels

We analyzed the cross-correlation between the global oscillations in the channels at each multi-channel condition to study whether channels were oscillating in sync with each other (either in-phase or with a phase delay between channels). The non-sinusoidal nature and the general lack of agreement between peak locations among channels operating together suggests that the channels are likely not oscillating with any sort of correlation between each other, and our results showed that to be true. Even for conditions where the peaks on the PSDs appeared in to be at the same frequency, the brightness of the discharge channels showed no correlation at any phase delay. This indicates that the oscillations between channels did not interact in any significant or meaningful way, a result which differs from previous work on

Table 4 Average value and standard deviation of both low and high oscillation frequencies for the three channels of the X3 across all operating conditions.

Channel	Low-freq.		High-freq.	
	Avg.	Std. Dev.	Avg.	Std. Dev.
Inner	12.5 kHz	3.9 kHz	74.0 kHz	10.0 kHz
Middle	12.7 kHz	2.7 kHz	63.0 kHz	12.0 kHz
Outer	12.4 kHz	3.2 kHz	50.8 kHz	4.6 kHz

the X2 two-channel NHT. A study by McDonald showed that for that thruster in certain operating conditions, the low-frequency peak of the outer channel would “bleed over” and appear in the inner channel’s PSD trace (though the inner channel’s peak never appeared in the outer channel’s PSD trace) [28]. No explanation was found for this behavior on the X2, and it is unclear from our work whether this type of phenomenon would appear for the X3 under certain operating conditions.

3. Oscillation Peak Frequencies

As demonstrated in the above example data, the oscillations of all three channels of the X3 are typically characterized by a low-frequency peak on the order of 10 kHz and a high-frequency peak on the order of 50-80 kHz. To understand how these frequencies vary by channel, we present in Table 4 the average frequencies and the standard deviation for both the low- and high-frequency peak for all three channels of the X3. These data are for the full set of operating conditions.

The low-frequency peak was very similar in characteristics for all three channels. The average frequency varied by less than 0.5 kHz between the three channels, and the standard deviation for all was less than 4 kHz, indicating that the frequency values were tightly clustered. (However, it is worth emphasizing that although the average frequency was very similar between the three channels, the actual values when multiple channels were operating simultaneously were not in perfect agreement, as discussed in the above section). The high-frequency peak, however, was less similar between channels. The average frequency was highest for the Inner channel at 74.0 kHz and lowest for the Outer at 50.8 kHz. The standard deviation also indicates that conditions were more closely clustered for the Outer than for the Inner or Middle channels. The comparatively large standard deviations for the Inner and Middle channels indicate that the location of the high-frequency peak varied more between different operating conditions.

4. Atypical Conditions

The vast majority of operating conditions across the entire range of X3 operation reported here had HSC results very similar to those we presented above. However, three test conditions exhibited HSC data that was, in various ways, atypical. These included two conditions that exhibited strongly sinusoidal breathing oscillations and one that included low-frequency (sub-kilohertz) spikes in discharge channel brightness superimposed on otherwise typical oscillations. Further details of these three cases are provided by Hall in Reference [1]. For all three of these outlier cases the

thruster performance did not fall out of family from other test points at similar conditions. More work is necessary to fully understand the reasons that the oscillation mode of the thruster would occasionally change, but it is nonetheless encouraging to see that thruster performance was not adversely affected when character of the oscillations changed.

5. Verification via High-Speed Discharge Current Analysis

Additionally, at each performance test point we collected high-speed discharge current measurements using the current probes and oscilloscopes described above. These measurements were triggered by the HSC data acquisition and thus are synchronized to those data. We applied a fast Fourier transform to these results as well, and from that calculated a PSD. These PSDs can only study the $m = 0$ global oscillation mode since no spatial information is known. However, we can compare these results to those from the HSC analysis as a verification of the HSC technique. Indeed, we found that for all test conditions, including those that were atypical, the HSDC analysis provided similar results as the HSC analysis for peak locations, widths, and relative heights. Further detail and example plots are provided by Hall [1]. We take the strong similarity between the two results, including the capturing of the atypical features of certain conditions, as a verification of the HSC technique.

V. Comparison of Single-channel and Multi-channel Operation

A. Performance

With three discharge channels operating in close proximity, there is the expectation that coupling between the channels could affect performance. Indeed, previous experiments with the X2 10-kW two-channel NHT demonstrated that that device produces increased thrust of up to 11% when operating both channels simultaneously as compared to the sum of each channel operating individually. A recent experiment investigated this phenomenon in more detail and found that the thrust increase was replicated when flowing propellant through the non-firing channel in single-channel mode [29]. This effect, and the changes observed in the plasma found to be causing the increase in thrust, were attributed to the change in the neutral pressure field close to the thruster caused by the flow from the adjacent channel. Beal identified similar trends in a cluster of 200-W Hall thrusters, finding that a single thruster could couple normally with a cathode on the opposite side of the two-thruster cluster if propellant was flowing through the intermediate thruster [30]. Plasma plume measurements suggested that this extra neutral flow was likely improving electron transport across field lines via collisional effects. Unfortunately, thrust was not measured in that study, so it is unclear whether there was a performance effect due to the increased local neutral pressure.

Here, we operated the X3 in its single- and three-channel configurations for seven different combinations of discharge voltage and current density. Figure 6 presents the thrust produced by the X3 at each of its IMO-configuration points alongside the summed thrust from the I, M, and O configurations at the same discharge voltage and current density. Note that although the power was constant for each condition, the magnetic field strength was optimized and thus

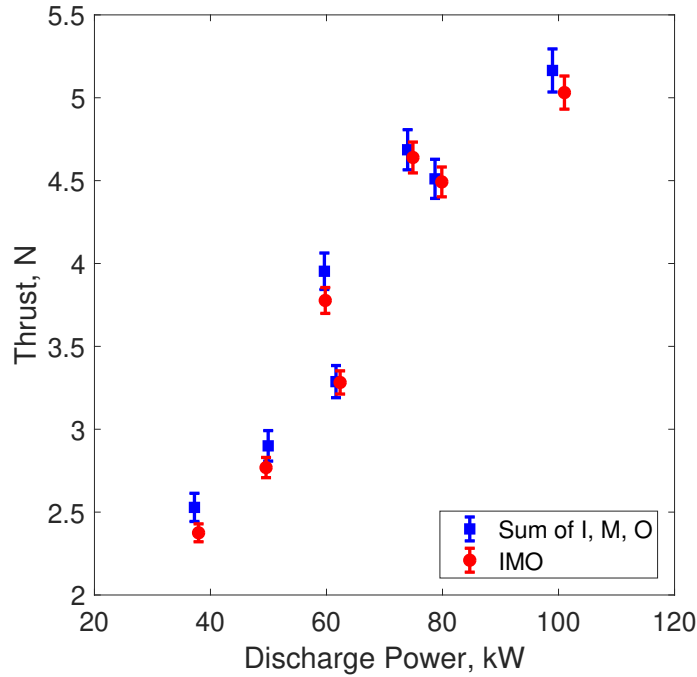


Fig. 6 Comparison of three-channel thrust and comparable summed single-channel thrusts for the X3.

varied (no more than 30%, as noted above). Additionally, individual channels were operated with only their respective electromagnets. Thus, these comparisons consist of individually optimized conditions.

Error bars reflect the thrust measurement uncertainty for each point, typically around 2%. We found that the summed I, M, and O conditions typically produced slightly more thrust than the IMO condition, but that in general the measurements matched to within their uncertainty. This result is notably different than that found on the X2 thruster, and further research is necessary to understand the reasons behind the difference in operation.

B. Oscillatory Behavior

In addition to the high-speed measurements described above, we collected peak-to-peak (P2P) and root-mean-square (RMS) measurements of the discharge current oscillations during this performance mapping campaign. These measurements were made by the clamp-on current probes and oscilloscopes and read by the data logger during telemetry measurement cycles. The values presented here are averaged over the same 60 second period as the telemetry used in the performance calculations. For simplicity, only the P2P values are presented. The RMS values showed similar trends between conditions but in all cases were a smaller percentage of the mean discharge current. Figure 7a presents the P2P values normalized by their respective channel’s mean discharge current. Single- and multi-channel conditions are indicated by closed and open markers, respectively. Figures 7b–d show the average values for each channel in single- and multi-channel operation for each discharge voltage tested. The error bars on the bar charts represent the standard

deviation of the values for each case.

The figures show that P2P values for all three channels were less than 40% for single-channel operation at all discharge voltages. The Outer channel's oscillation strength typically was unchanged or grew slightly ($< 10\%$) in multi-channel operation but remained below 50% for all but a single condition (at 500 V). The Middle channel's oscillation strength grew slightly more in multi-channel operation, rising to an average of about 50% for 300 V and 400 V and closer to 75% for 500 V. The Inner channel experienced the largest difference in oscillation strength between single-channel and multi-channel operation, rising from a single-channel average less than 40% the mean values (comparable to the other two channels) to a multi-channel average approximately 70% at 300 V and 400 V and an average approaching 100% at 500 V.

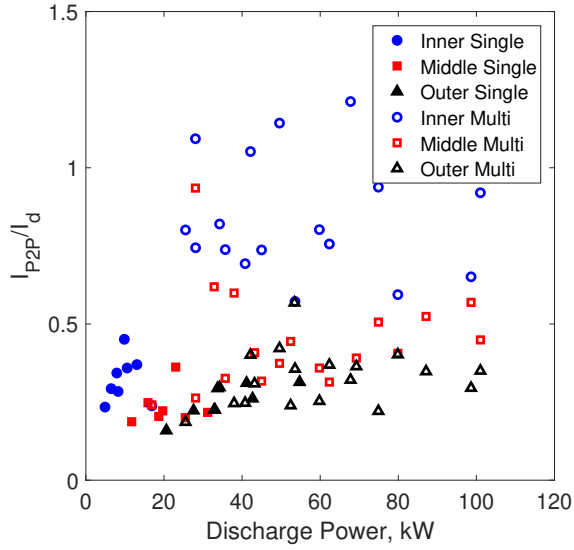
These results indicate the relative strength of the discharge oscillations varied as a function of thruster operating mode (single- versus multi-channel). However, as noted above, the HSC results indicated that the mode of operation, described as a breathing-type $m=0$ mode with little spoke content and a pair of peaks at approximately 10 kHz and 60-80 kHz, did not vary significantly between operating modes.

C. Cathode Coupling

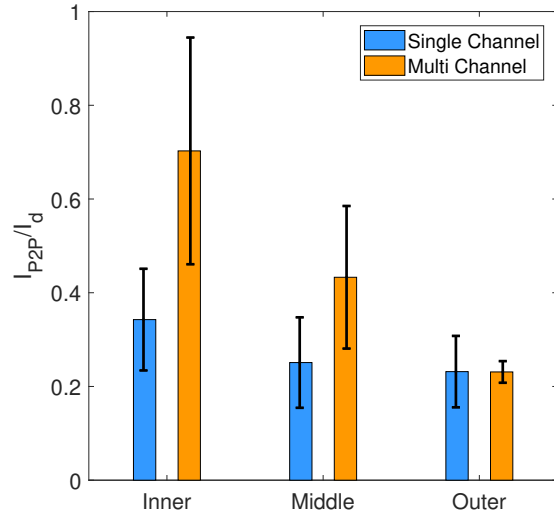
Another metric to compare the operation of the X3 in single-channel and multi-channel modes is the cathode-to-ground voltage (V_{cg}). Hall thruster cathode-to-ground voltages are typically between 5 and 30 V below facility ground, and is a metric of how well the thruster is coupling to the cathode [31]. Values of V_{cg} that are smaller magnitude (less negative) are indicative of improved coupling, and these smaller values allow for more of the thruster discharge voltage to be available for ion beam acceleration. Substantial differences in V_{cg} between single- and multi-channel conditions for the X3 would indicate that the thruster is coupling to the cathode differently between these conditions. Figure 8 presents V_{cg} for both single- and multi-channel X3 operation as a function of discharge power. The TCFE was held at 7% of the anode flow for all test points here except one; this test point, at 5%, featured a V_{cg} of -10.9 V, very near the mean value of the 7% TCFE conditions. The data show that V_{cg} varied between -8 and -14 V across all conditions and power levels tested here, showing no significant difference between single- and multi-channel operation and demonstrating no trend with discharge power.

VI. Conclusions

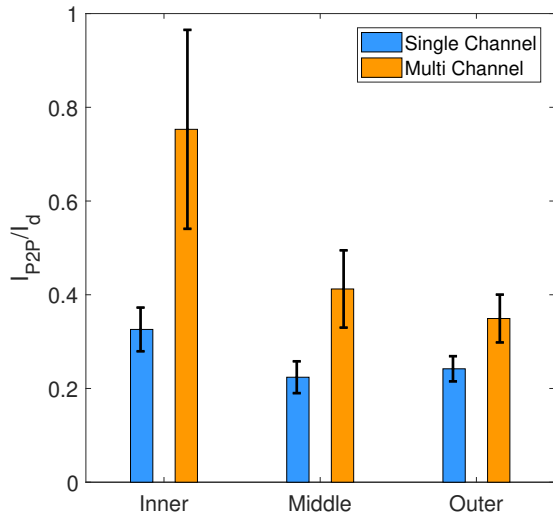
We successfully measured the performance of the X3 for a range of conditions spanning total thruster input power levels from 5 to 102 kW. These conditions consisted of discharge voltages from 300 to 500 V and current densities that were 0.63, 1.00, and 1.26 of a reference value. The seven channel combinations of the thruster were throttled across this range of settings. For each test point, we directly measured thrust using a high-power inverted-pendulum thrust stand, and from those thrust measurements and thrust telemetry, we calculated specific impulse and efficiency values. We



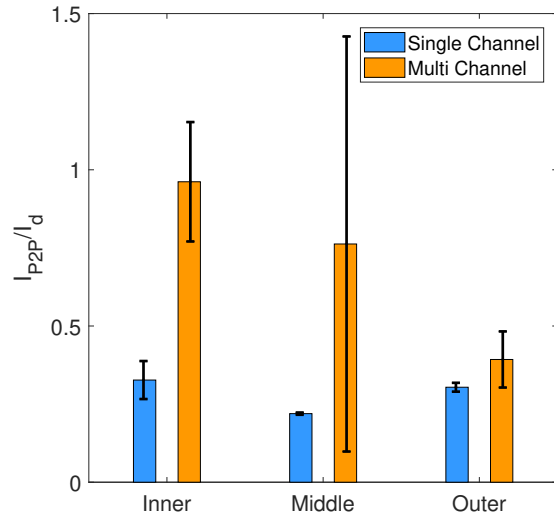
(a) P2P versus discharge power for all test conditions.



(b) 300 V average P2P values for each channel in single- and multi-channel operation.



(c) 400 V average P2P values for each channel in single- and multi-channel operation.



(d) 500 V average P2P values for each channel in single- and multi-channel operation.

Fig. 7 Peak-to-peak discharge current oscillation values normalized by the mean discharge current for that channel. Error bars on bar charts represent standard deviation of data.

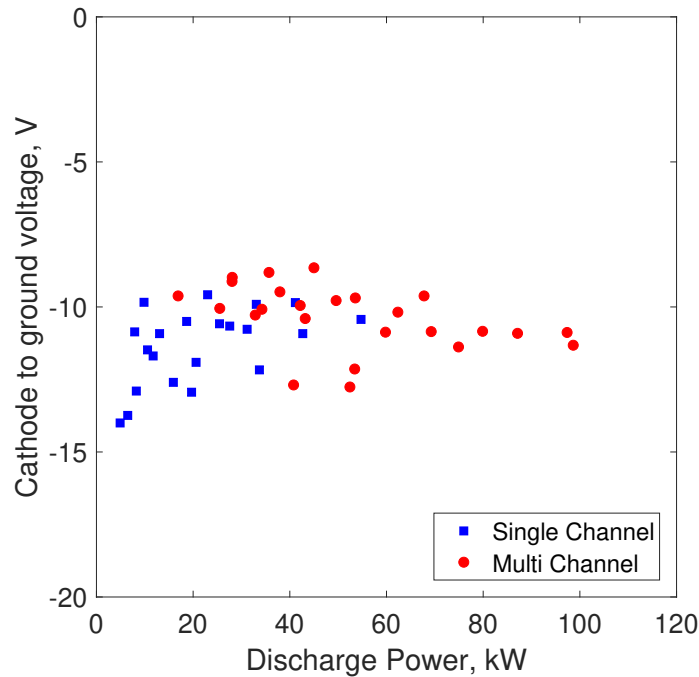


Fig. 8 Cathode-to-ground voltage versus discharge power for all test conditions. Single- and multi-channel conditions are noted by square and circle markers, respectively.

collected measurements of the discharge current oscillations at each point to assess thruster stability, which included P2P measurements of the oscillations as well as HSC measurements. The HSC data were used to assess the discharge oscillation behavior of the thruster in detail.

Our results demonstrated that a three-channel 100-kW class NHT can offer comparable or even improved performance over high-power single-channel thrusters. The X3 demonstrated total efficiencies ranging from 0.54–0.67 and total specific impulses from 1800–2650 seconds, experiencing the peak efficiency at 500 V discharge voltage. Additionally, the results indicate that none of the available channel combinations were significantly over- or under-performing the rest, demonstrating comparable specific impulse and efficiency at a fixed discharge voltage and current density. High-speed camera results indicated that for a vast majority of conditions, all channels of the X3 were oscillating in a breathing-type mode characterized by stochastic (non-sinusoidal) oscillations that were not correlated to those occurring in adjacent channels. The oscillation behavior was mostly unchanged between single- and multi-channel operation.

These results differed from previous NHT results in two key ways. First, the sum of the single-channel thrusts generally was not significantly different than the three channels operating together for a given discharge voltage and current density. Second, the channels showed no indication of oscillating in conjunction with each other when operating together, with no correlation between oscillation strength or frequency and no signs of “bleed over” from one channel to the other of any spectral content. These differences make clear that further understanding of the physics of general NHT

Table 5 300 V throttle table for the X3 performance measurements.

$V_{d,I}$ V	$I_{d,I}$ A	$V_{d,M}$ V	$I_{d,M}$ A	$V_{d,O}$ V	$I_{d,O}$ A	$P_{d,t}$ kW	T N	$I_{sp,a}$ s	$I_{sp,t}$ s	η_a -	η_t -	V_{cg} V	P_b μ Torr
300.2	16.3	0	0	0	0	4.9	0.35	1950	1820	0.69	0.64	-14.0	4.6
0	0	296.4	39.6	0	0	11.7	0.82	1950	1830	0.67	0.62	-11.7	10.2
0	0	0	0	300.3	68.6	20.6	1.35	2070	1950	0.67	0.62	-11.9	15.9
300.0	16.5	301.0	39.7	0	0	16.9	1.15	1930	1800	0.65	0.60	-9.6	13.8
300.0	16.0	0	0	300.4	68.9	25.5	1.63	2060	1940	0.65	0.60	-10.1	18.5
0	0	303.3	39.0	300.3	70.0	32.9	2.12	2100	1870	0.66	0.58	-10.3	23.0
299.8	16.5	303.1	39.4	300.3	70.1	37.9	2.38	2040	1920	0.63	0.58	-9.5	25.5
299.5	26.4	0	0	0	0	7.9	0.56	2050	1920	0.71	0.66	-10.9	6.6
0	0	292.6	63.8	0	0	18.7	1.28	2060	1930	0.70	0.64	-10.5	14.5
0	0	0	0	300.2	110.2	33.1	2.11	2150	2010	0.67	0.62	-9.9	22.9
299.3	27.5	300.4	66.1	0	0	28.1	1.85	2100	1960	0.68	0.63	-9.0	19.7
299.3	25.4	0	0	300.1	110.5	40.8	2.58	2110	2030	0.65	0.62	-12.7	26.0
0	0	305.1	63.1	300.0	110.6	52.4	3.30	2102	2002	0.65	0.61	-12.8	31.9
299.1	25.7	304.6	62.4	300.0	110.0	60.0	3.74	2070	1970	0.63	0.60	-14.4	36.2
298.9	32.9	0	0	0	0	9.84	0.66	2040	1910	0.67	0.62	-9.8	7.5
0	0	288.1	79.84	0	0	23.00	1.48	1950	1820	0.62	0.57	-9.6	17.0
0	0	0	0	299.3	137.5	41.2	2.55	2150	2010	0.65	0.61	-9.9	27.2
298.4	33.6	300.1	78.6	298.1	138.5	74.9	4.64	2130	2020	0.65	0.61	-11.4	42.2

operation—beyond that of a small number of devices—is critical to the further development of the technology for potential application on future, high-power missions.

Ultimately, the X3 demonstrated new levels of Hall thruster power (102 kW), thrust (5.4 N), and discharge current (247 A). Though many questions remain, these results demonstrate the capability of Hall thrusters and specifically NHTs for cargo and crew transport applications and show that the X3 represents a significant milestone on the roadmap to deep-space destinations such as Mars.

Acknowledgments

At the time of this work, Scott J. Hall was supported by a NASA Space Technology Research Fellowship under grant number NNX14AL67H. Sarah E. Cusson and Matthew J. Baird are supported by NASA Space Technology Research Fellowships under grant numbers NNX15AQ43H and NNX16AM96H. A portion of the work described here was performed as a part of NASA’s NextSTEP program under grant number NNH16CP17C. The authors would like to acknowledge a number of personnel at NASA Glenn Research Center who contributed to this work, including Eric Pencil, Luis Piñero, Chad Joppeck, Taylor Varouh, Nick Lalli, Richard Senyitko, Jim Zakany, Jim Szelogowski, Kevin Blake, Josh Gibson, Larry Hambly, George Jacynycz, and Dave Yendriga. Finally, the authors gratefully acknowledge Dan M. Goebel of NASA JPL for developing and providing the cathode used in this experiment, as well as for his technical insight.

Appendix

Table 6 400 V throttle table for the X3 performance measurements.

$V_{d,I}$ V	$I_{d,I}$ A	$V_{d,M}$ V	$I_{d,M}$ A	$V_{d,O}$ V	$I_{d,O}$ A	$P_{d,t}$ kW	T N	$I_{sp,a}$ s	$I_{sp,t}$ s	η_a –	η_t –	V_{cg} V	P_b μ Torr
400.4	16.2	0	0	0	0	6.5	0.39	2190	2050	0.64	0.59	-13.7	4.3
0	0	400.1	39.8	0	0	15.9	0.93	2210	2060	0.63	0.59	-12.6	9.7
0	0	0	0	400.0	68.9	27.6	1.58	2360	2200	0.66	0.61	-10.7	15.9
400.2	16.9	0	0	399.7	68.8	34.2	1.94	2380	2220	0.66	0.61	-10.1	18.5
0	0	394.8	38.9	399.6	69.7	43.2	2.45	2350	2200	0.65	0.61	-10.4	23.0
400.1	16.5	394.4	39.3	399.6	68.8	49.5	2.77	2310	2160	0.63	0.59	-9.8	25.6
399.77	26.4	0	0	0	0	10.6	0.61	2290	2140	0.65	0.60	-11.48	6.3
0	0	399.5	63.7	0	0	25.5	1.49	2360	2210	0.68	0.63	-10.6	14.1
0	0	0	0	399.1	106.9	42.7	2.40	2450	2330	0.68	0.64	-10.9	22.0
399.6	25.9	399.5	63.4	0	0	35.7	2.07	2420	2270	0.69	0.64	-8.8	19.0
399.7	25.0	0	0	399.8	109.0	53.6	2.98	2450	2290	0.67	0.62	-9.7	26.6
0	0	393.0	64.6	399.7	109.8	69.3	3.94	2460	2300	0.69	0.64	-10.8	32.6
399.5	25.7	401.0	64.1	399.6	109.9	79.9	4.49	2440	2240	0.67	0.61	-10.8	37.0
398.6	33.8	402.7	76.1	398.2	136.9	98.6	5.42	2470	2340	0.67	0.63	-11.3	41.8

Table 7 500 V throttle table for the X3 performance measurements.

$V_{d,I}$ V	$I_{d,I}$ A	$V_{d,M}$ V	$I_{d,M}$ A	$V_{d,O}$ V	$I_{d,O}$ A	$P_{d,t}$ kW	T N	$I_{sp,a}$ s	$I_{sp,t}$ s	η_a –	η_t –	V_{cg} V	P_b μ Torr
500.7	16.5	0	0	0	0	8.2	0.43	2460	2300	0.64	0.59	-12.9	4.4
0	0	500.9	39.3	0	0	19.7	1.08	2590	2420	0.70	0.64	-12.9	9.9
0	0	0	0	500.4	67.4	33.7	1.77	2770	2580	0.71	0.66	-12.2	14.7
500.5	17.0	500.6	39.1	0	0	38.0	1.37	2450	2290	0.59	0.54	-9.1	12.6
500.4	16.8	0	0	500.3	67.5	42.2	2.19	2740	2560	0.70	0.64	-9.9	17.8
0	0	508.6	37.3	500.6	68.8	53.4	2.62	2790	2590	0.67	0.61	-12.1	20.7
500.2	18.0	499.2	38.1	500.6	68.6	62.4	3.28	2760	2580	0.71	0.66	-10.2	25.1
500.1	26.1	0	0	0	0	13.1	0.70	2680	2500	0.71	0.66	-10.9	6.2
0	0	500.4	62.3	0	0	31.2	1.69	2710	2530	0.72	0.67	-10.8	14.0
0	0	0	0	499.6	109.5	54.7	2.77	2840	2650	0.70	0.65	-10.4	21.9
499.9	26.3	499.8	63.7	0	0	45.0	2.34	2720	2540	0.69	0.64	-8.7	18.5
499.8	26.2	0	0	500.7	109.2	67.8	3.38	2800	2610	0.68	0.63	-9.6	25.3
0	0	504.3	63.8	499.4	110.0	87.1	4.34	2740	2560	0.67	0.62	-10.9	32.2
499.4	28.2	505.3	63.2	499.6	110.1	101.0	5.03	2750	2570	0.67	0.63	-10.3	35.9

References

- [1] Hall, S. J., “Characterization of a 100-kW Class Nested-Channel Hall Thruster,” Ph.D. Dissertation, University of Michigan, Ann Arbor, MI, 2018.
- [2] Hofer, R. R., and Randolph, T. M., “Mass and Cost Model for Selecting Thruster Size in Electric Propulsion Systems,” *Journal of Propulsion and Power*, Vol. 29, No. 1, 2012, pp. 166–177. <https://doi.org/10.2514/1.B34525>.
- [3] Goebel, D. M., Jameson, K. K., and Hofer, R. R., “Hall Thruster Cathode Flow Impact on Coupling Voltage and Cathode Life,” *Journal of Propulsion and Power*, Vol. 28, No. 2, 2012, pp. 355–363. <https://doi.org/10.2514/1.B34275>.
- [4] Manzella, D., “Scaling Hall Thrusters to High Power,” Ph.D. Dissertation, Stanford University, Stanford, CA, 2005.
- [5] Soulas, G., Haag, T., Herman, D., and Huang, W., “Performance Test Results of the NASA-457M v2 Hall Thruster,” *48th AIAA Joint Propulsion Conference*, AIAA Paper 2012-3940, Atlanta, GA, 2012. <https://doi.org/10.2514/6.2012-3940>.
- [6] Kamhawi, H., Haag, T. W., Jacobson, D. T., and Manzella, D. H., “Performance Evaluation of the NASA-300M 20 kW Hall Effect Thruster,” *47th AIAA/ASME/SAE/ASEE Joint Propulsion Conference and Exhibit*, AIAA Paper 2011-5521, San Diego, CA, 2011. <https://doi.org/10.2514/6.2011-5521>.
- [7] Peterson, P. Y., Jacobson, D. T., Manzella, D. H., and John, J. W., “The Performance and Wear Characterization of a High-power High-Isp NASA Hall Thruster,” *41st AIAA/SAE/ASEE Joint Propulsion Conference*, AIAA Paper 2005-4243, Tuscon, AZ, 2005. <https://doi.org/10.2514/6.2005-4243>.
- [8] Spores, R., Monheiser, J., Dempsey, B. P., Wade, D., Creel, K., Jacobson, D., and Drummond, G., “A Solar Electric Propulsion Cargo Vehicle to Support NASA Lunar Exploration Program,” *25th International Electric Propulsion Conference*, Electric Rocket Propulsion Society, Paper IEPC-2005-320, Princeton, NJ, 2005.

- [9] Szabo, J., Pote, B., Hruby, V., Byrne, L., Tedrake, R., Kolencik, G., Kamhawi, H., and Haag, T. W., "A Commercial One Newton Hall Effect Thruster for High Power In-Space Missions," *47th AIAA/ASME/SAE/ASEE Joint Propulsion Conference*, AIAA Paper 2011-6152, San Diego, CA, 2011. <https://doi.org/10.2514/6.2011-6152>.
- [10] Liang, R., "The Combination of Two Concentric Discharge Channels into a Nested Hall-Effect Thruster," Ph.D. Dissertation, University of Michigan, Ann Arbor, MI, 2013.
- [11] Florenz, R. E., "The X3 100-kW Class Nested-Channel Hall Thruster: Motivation, Implementation, and Initial Performance," Ph.D. thesis, University of Michigan, Ann Arbor, MI, 2013.
- [12] Hall, S. J., Jorns, B. A., Gallimore, A. D., Kamhawi, H., Haag, T. W., Mackey, J. A., Gilland, J. H., Peterson, P. Y., and Baird, M. J., "High-Power Performance of a 100-kW Class Nested Hall Thruster," *35th International Electric Propulsion Conference*, Atlanta, GA, Electric Rocket Propulsion Society, Paper IEPC-2017-228, Atlanta, GA, 2017.
- [13] Hall, S. J., Jorns, B. A., Gallimore, A. D., Kamhawi, H., and Huang, W., "Plasma Plume Characterization of a 100-kW Nested Hall Thruster," *Journal of Propulsion and Power*, 2020. (not yet published).
- [14] Chu, E., Goebel, D. M., and Wirz, R. E., "Reduction of Energetic Ion Production in Hollow Cathodes by External Gas Injection," *Journal of Propulsion and Power*, Vol. 29, No. 5, 2013, pp. 1155–1163. <https://doi.org/10.2514/1.B34799>.
- [15] Hall, S. J., Jorns, B. A., Gallimore, A. D., and Goebel, D. M., "Operation of a High-Power Nested Hall Thruster With Reduced Cathode Flow Fraction," *Journal of Propulsion and Power*, 2020. (not yet published).
- [16] Dankanich, J. W., Walker, M., Swiatek, M. W., and Yim, J. T., "Recommended Practice for Pressure Measurement and Calculation of Effective Pumping Speed in Electric Propulsion Testing," *Journal of Propulsion and Power*, Vol. 33, No. 3, 2017, pp. 668–680. <https://doi.org/10.2514/1.B35478>.
- [17] Haag, T., "Thrust Stand for High-Powered Electric Propulsion Devices," *Review of Scientific Instruments*, Vol. 62, No. 1186, 1991. <https://doi.org/10.1063/1.1141998>.
- [18] Xu, K. G., and Walker, M. L., "High-power, Null-type, Inverted Pendulum Thrust Stand," *Review of Scientific Instruments*, Vol. 80, No. 5, 2009, p. 055103. <https://doi.org/10.1063/1.3125626>.
- [19] Polk, J. E., Pancotti, A., Haag, T., King, S., Walker, M., Blakely, J., and Ziemer, J., "Recommended Practice for Thrust Measurement in Electric Propulsion Testing," *Journal of Propulsion and Power*, Vol. 33, No. 3, 2017, pp. 539–555. <https://doi.org/10.2514/1.B35564>.
- [20] Choueiri, E. Y., "Plasma Oscillations in Hall Thrusters," *Physics of Plasmas*, Vol. 8, No. 4, 2001, pp. 1411–1426. <https://doi.org/10.1063/1.1354644>.
- [21] McDonald, M. S., and Gallimore, A. D., "Rotating Spoke Instabilities in Hall Thrusters," *IEEE Transactions on Plasma Science*, Vol. 39, No. 11, 2011, pp. 2952–2953. <https://doi.org/10.1109/TPS.2011.2161343>.

- [22] Sekerak, M. J., “Plasma Oscillations and Operational Modes in Hall Effect Thrusters,” Ph.D. Dissertation, University of Michigan, Ann Arbor, MI, 2014.
- [23] Jorns, B. A., and Hofer, R. R., “Plasma Oscillations in a 6-kW Magnetically Shielded Hall Thruster,” *Physics of Plasmas*, Vol. 21, No. 5, 2014, p. 053512. <https://doi.org/10.1063/1.4879819>.
- [24] Sekerak, M. J., Gallimore, A. D., Brown, D. L., Hofer, R. R., and Polk, J. E., “Mode Transitions in Hall-Effect Thrusters Induced by Variable Magnetic Field Strength,” *Journal of Propulsion and Power*, Vol. 32, No. 4, 2016, pp. 903–917. <https://doi.org/10.2514/1.B35709>.
- [25] McDonald, M. S., “Electron Transport in Hall Thrusters,” Ph.D. Dissertation, University of Michigan, Ann Arbor, MI, 2012.
- [26] Ellison, C. L., Raitses, Y., and Fisch, N. J., “Cross-field Electron Transport Induced by a Rotating Spoke in a Cylindrical Hall Thruster,” *Physics of Plasmas*, Vol. 19, No. 1, 2012, p. 013503. <https://doi.org/10.1063/1.3671920>.
- [27] Goebel, D. M., Jameson, K. K., Katz, I., and Mikellides, I. G., “Potential Fluctuations and Energetic Ion Production in Hollow Cathode Discharges,” *Physics of Plasmas*, Vol. 14, No. 10, 2007, p. 103508. <https://doi.org/10.1063/1.2784460>.
- [28] McDonald, M. S., Sekerak, M. J., Gallimore, A. D., and Hofer, R. R., “Plasma Oscillation Effects on Nested Hall Thruster Operation and Stability,” *2013 IEEE Aerospace Conference*, IEEE, Big Sky, MT, 2013. <https://doi.org/10.1109/AERO.2013.6497190>.
- [29] Cusson, S. E., Georjgin, M. P., Dragnea, H. C., Dale, E. T., Dhaliwal, V., Boyd, I. D., and Gallimore, A. D., “On Channel Interactions in Nested Hall Thrusters,” *Journal of Applied Physics*, Vol. 123, No. 13, 2018, p. 133303. <https://doi.org/10.1063/1.5028271>.
- [30] Beal, B. E., Gallimore, A. D., and Hargus, W. A., “Effects of Cathode Configuration on Hall Thruster Cluster Plume Properties,” *Journal of Propulsion and Power*, Vol. 23, No. 4, 2007, pp. 836–844. <https://doi.org/10.2514/1.24636>.
- [31] Sommerville, J. D., and King, L. B., “Hall-Effect Thruster–Cathode Coupling, Part I: Efficiency Improvements from an Extended Outer Pole,” *Journal of Propulsion and Power*, Vol. 27, No. 4, 2011, pp. 744–753. <https://doi.org/10.2514/1.50123>.